ACS APPLIED MATERIALS & INTERFACES

RESEARCH ARTICLE

www.acsami.org

High-Efficiency, Solid-State, Dye-Sensitized Solar Cells Using Hierarchically Structured TiO_2 Nanofibers

Daesub Hwang,[†] Seong Mu Jo,[†] Dong Young Kim,[†] Vanessa Armel,[‡] Douglas R. MacFarlane,[‡] and Sung-Yeon Jang*[,†,§]

[†]Polymer Hybrids Center, Korea Institute of Science and Technology, Seoul, Korea

[‡]Australian Centre for Electromaterials Science, School of Chemistry, Monash University, Clayton, VIC 3800, Australia

Supporting Information

ABSTRACT: High-performance, room-temperature (RT), solid-state dye-sensitized solar cells (DSSCs) were fabricated using hierarchically structured TiO_2 nanofiber (HS-NF) electrodes and plastic crystal (PC)-based solid-state electrolytes. The electrospun HS-NF photoelectrodes possessed a unique morphology in which submicrometer-scale core fibers are interconnected and the nanorods are dendrited onto the fibers. This nanorod-in-nanofiber morphology yielded porosity at both the mesopore and macropore level. The macropores, steming from the interfiber space, afforded high pore volumes to facilitate the infiltration of the PC electrolytes, whereas the mesoporous nanorod dendrites offered high surface area for enhanced dye loading. The solid-state DSSCs using HS-NFs (DSSC-NF) demonstrated improved power conversion efficiency (PCE) compared to conventional TiO_2 nanoparticle (NP) based DSSCs (DSSC-NP). The improved performance (>2-fold) of the DSSC-NFs was due to the reduced internal series resistance (R_s) and the enhanced charge recombination lifetime (τ_r) determined by electrochemical impedance spectroscopy and intensity modulated photocurrent/photovoltage spectroscopy. The easy penetration of the PC electrolytes into HS-NF layers via the macropores reduces R_s significantly, improving the fill factor (FF) of the resulting DSSC-NFs. The τ_r difference between the DSSC-NF and DSSC-NP in the PC electrolytes was extraordinary (~ 14 times) compared to reported results in conventional organic liquid electrolytes. The optimized PCE of DSSC-NF using the PC electrolytes was 6.54, 7.69, and 7.93% at the light intensity of 100, 50, and 30 mW cm^{-2}, respectively, with increased charge collection efficiency (>40%). This is the best performing RT solid-state DSSC using a PC electrolyte. Considering the fact that most reported quasi-solid state or nonvolatile electrolytes require higher iodine contents for efficient ion transport, our HS-NFs are a promising morphology for such electrolytes that have limited ion mass transport.

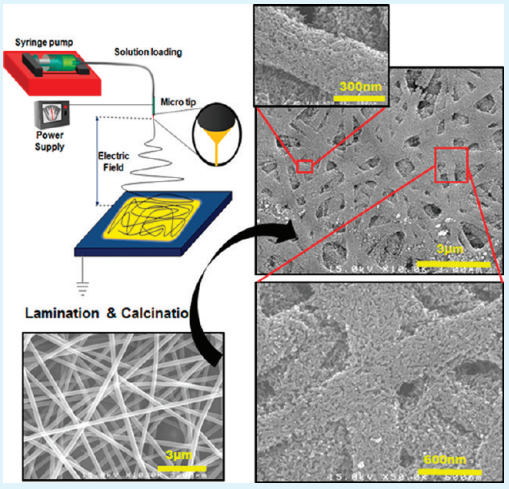

KEYWORDS: dye-sensitized solar cells, TiO_2 nanofibers, solid-state electrolytes, plastic crystal, charge recombination

INTRODUCTION

Dye-sensitized solar cells (DSSC) have attracted much attention as cost-effective devices that can convert sunlight into electrical energy. The technical development and scientific investigation of DSSCs in recent years have realized high power conversion efficiencies (PCE >11%).[1] In typical high-efficiency DSSCs, organic liquid electrolytes containing the I^-/I_3^- redox couple have been routinely used because of the demands for sufficient mass transport and fast dye regeneration. However, the use of liquid electrolytes limits the practical development of DSSCs, retarding their commercialization. Replacing the liquid electrolytes with solid-state electrolytes (SSE) has been considered as one of the crucial issues in order to fully capitalize on the merits of DSSCs, through improving their mechanical stability and simplifying fabrication processes, including the elimination of the need for hermetic sealing.[2−4] A number of approaches to the development of solid electrolytes have been attempted including organic/inorganic hole transport materials,[5−9] polymer-based gel electrolytes,[10−14] and physically cross-linked nanoparticle supported gel electrolytes.[15−17] Although a true solid-state DSSC could be attained using solid hole-transporting materials, their electronic transport ability was far less effective than the ionic transport in quasi solid-state gel type electrolytes with high ion concentration. Thus the resulting cell efficiency of the quasi-SSE based DSSCs has been superior.

The (quasi) SSEs often have relatively high viscosity prior to gelation, thus their infiltration into the conventional, mesoporous TiO_2 photoelectrodes consisting of nanoparticle (NP) layers (~10 μm thick) has been challenging. Furthermore, the high viscosity retards the mass transport of the ions, typically the

Received: January 24, 2011
Accepted: March 31, 2011
Published: March 31, 2011

I^-/I_3^- redox couple, in the electrolytes. Because of the impeded mass transport, the ion transport in (quasi) SSEs mainly relies in some cases on the Grotthus-type polyiodide bond exchange mechanism (GEM).[18−20] In this mechanism, the concentration and ratio of I^- to I_3^- plays a key role in efficient ion transport because the population of the polyiodide species is crucial. Therefore, much higher amounts of iodine are often required to generate the required high concentrations of the polyiodide species. On the other hand, increased iodine concentration is expected to render more efficient the unwanted recombination process of the injected photoelectrons with I_3^- in the electrolyte and also to produce additional losses due to visible light absorption by the electrolyte. This issue, coupled with the infiltration problem, has been one of the main reasons why the performance of (quasi) SSEs has not reached that of organic liquid electrolytes, although improved long-term stability of DSSCs using (quasi) SSEs has been shown recently.[10,11] Consequently, TiO_2 layers with controlled morphology that can facilitate the penetration of viscous electrolytes and provide lower recombination rates are essential to improve the performance of this important type of DSSCs.

One-dimensional (1D) nanostructured TiO_2-based DSSCs have demonstrated reduced recombination rates because of their low junction density compared to the conventional TiO_2−NP based DSSCs.[21−24] In our earlier work, 1D TiO_2 nanorods prepared by an electrospinning (e-spinning) method demonstrated that ∼40% enhanced efficiency compared to conventional TiO_2−NP-based DSSCs in a conventional organic liquid electrolyte, due to the reduced charge recombination rate.[25] Most of the reported 1D TiO_2 nanostructures provide higher porosity and hence is expected to afford improved electrolyte penetration; however, this resulted in lower dye loadings because of the diminished surface area.[26−29] A 1D nanostructure morphology, which can offer large pore size, volumes, and high surface area, if such a combination is possible, would be the ideal structure to improve the performance of (quasi) solid-state DSSCs.

Herein, room-temperature (RT) solid-state DSSCs were fabricated using hierarchically structured TiO_2 nanofibers (HS-NF) as the photoelectrode layers along with a plastic crystal (PC) based solid electrolyte, P14II-SN. Use of PC-based electrolytes in DSSCs has been reported several times,[30−32] and relatively high efficiency (PCE of ∼5% under one sun illumination) was achieved by Grätzel and co-workers using TiO_2−NP-based photoelectrodes. The PC electrolyte exhibited elevated ionic conductivity and ion diffusion coefficients, which are even higher than those of ionic liquid (IL) based electrolytes.[30] However, the performance of the corresponding DSSCs was not remarkable, with relatively low open circuit voltage (V_{OC} = 618 mV) despite the premium properties of the PC electrolyte. In this report, RT solid-state DSSCs using HS-NFs (DSSC-NF) were fabricated and the performance was compared to the conventional NP based solid-state DSSCs (DSSC-NP). Our HS-NFs had nanorod-in-nanofiber morphology, and the resulting photoelectrode layers present pores in two distinct size domains; macropores facilitate penetration of the viscous molten PC electrolytes, while the mesopores offer high surface area for high levels of dye adsorption. The DSSC-NFs exhibited more than two times higher PCE than the equivalent DSSC-NPs, with reduced internal series resistance (R_S) and charge recombination rate. The R_S of DSSC-NFs determined by electrochemical impedance spectroscopy (EIS) was >2-fold lower than that of DSSC-NPs. The enhancement of the charge recombination lifetime (τ_r) of our DSSC-NFs determined by intensity modulated photovoltage spectroscopy (IMVS) was remarkable. This extraordinary enhancement of the τ_r is attributed to the morphological effects of our HS-NFs, because the facilitated charge recombination in the PC electrolytes that stems from the increased amount of I_3^- ions was effectively retarded by the much lower junction density of HS-NFs. The superior morphological effects of HS-NFs was reflected in the performance of DSSCs, and the optimized PCE of RT solid-state DSSC-NF was 6.54% with increased V_{OC} (668 mV) under AM 1.5G one sun condition and 7.93% under 30 mW cm^{-2} illumination. This is a significant improvement compared to the previous highest reported value (∼5% at AM 1.5G and 6.7% under 52 mW cm^{-2}) of PC based solid-state DSSCs revealing that the hierarchical 1D nanostructured TiO_2 is the ideal morphology for the (quasi) SSEs that have limited mass-transport properties.

EXPERIMENTAL SECTION

Preparation of Hierarchically Structured TiO_2 Nanofibers (HS-NFs). The TiO_2/polymer nanofibers were electrospun directly onto a SnO_2:F-coated glass substrate 10 cm ×10 cm (TEC-15, Pilkington). The precursor composite solution consists of 8 wt % poly(vinyl acetate) (PVAc) in dimethyl formamide (DMF), 0.25 M titanium(IV) propoxide (Aldrich), and 0.1 M acetic acid as a catalyst. The precursor solution was loaded into a syringe and connected to a high-voltage power supply (205B-50R, Bertan). An electric field of 1.4 kV cm^{-1} was applied. Then, the as-spun TiO_2 web was pressed using hot-plastes at 120 °C for 10 min under a pressure of 12.8 MPa. Finally, the pressed TiO_2 photoelectrode was calcined to remove polymers and to develop the anatase phase HS-NFs in a stepwise fashion (15 min at 150 °C, 15 min at 320 °C, and 30 min at 450 °C).

Preparation of Nonstructured TiO_2 Nanoparticles. The TiO_2 nanoparticles (NS-NPs) based photoelectrodes were prepared using the doctor-blade method. Specifically, the TiO_2 colloidal solution (P25, Degussa) was spread onto a FTO substrate using a doctor-blade coater. The porosity was controlled by adding the 20 wt % poly(ethylene glycol) (Aldrich, average MW = 10 000 g/mol) and 20 wt % poly-(ethylene oxide) (Aldrich, average MW = 100 000 g/mol) to the TiO_2 colloidal solution.

Device Fabrication. After post-treatment with 0.05 M $TiCl_4$ for 20 min at 80 °C, the TiO_2 films were rinsed with water and then sintered at 450 °C for 30 min. After cooling to 80 °C, the TiO_2 electrodes were immersed into the purified 3×10^{-4} M *cis*-di (thiocyanato)-*N,N′*-bis (2,2′-bipyridyl-4-carboxylic acid-4′-tetrabutylammonium carboxylate) ruthenium(II) (N719, Solaronix) solution for 15 h at room temperature.

For the counter electrode, the FTO plates were drilled by microdrill, washed with 0.1 M HCl solution in ethanol, and then subsequently cleaned in an ultrasonic bath with water and ethanol for 15 min. A Pt counter electrode was prepared by drop casting of 5 mM H_2PtCl_6 in isopropyl alcohol onto the washed FTO plates and then sintered at 400 °C for 20 min under air conditions. The dye-adsorbed TiO_2 electrodes were rinsed with ethanol and dried under nitrogen flow. The dye-adsorbed TiO_2 electrodes were assembled and sealed with the counter electrode using the thermal adhesive films (Surlyn, Dupont 1702, 25-μm-thick) as a spacer to produce sandwich-type cells. The plastic crystal electrolyte consisted of succinonitrile, iodine, 1-methyl-3-butyl pyrrolidine (P_{14}) 100: 1: 5 (mole ratio). The plastic crystal electrolyte was introduced at 70 °C through a drilled hole on the counter electrode. Finally, the holes were sealed with a hot-melt films and a cover glass.

Photovoltaic and Photoelectrical Measurements. Photovoltaic measurement of the DSSCs employed an AM 1.5 solar simulator

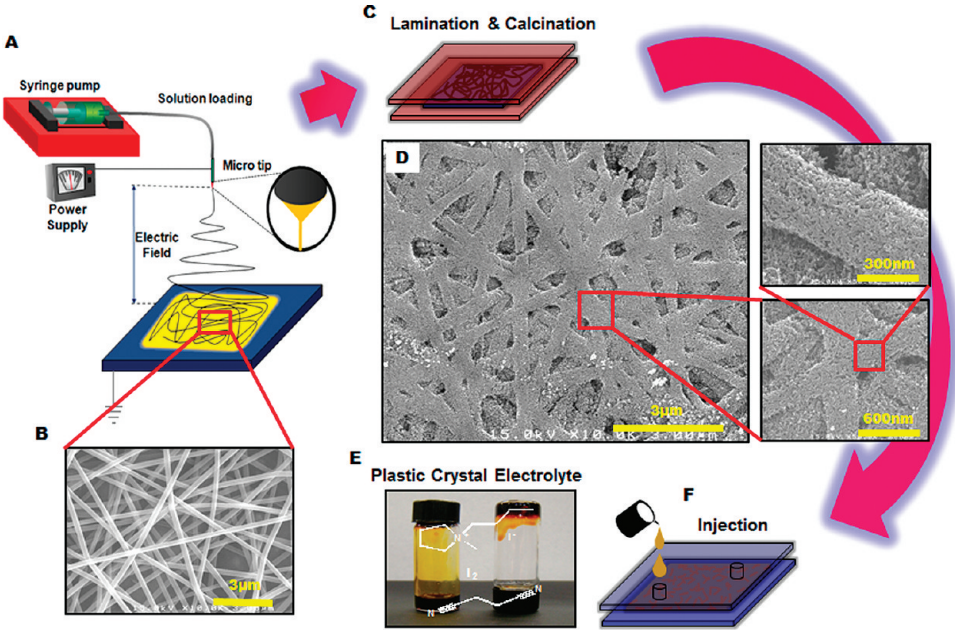

Figure 1. Schematic description of the fabrication of solid-state DSSCs using HS-NF photoelectrodes and PC-SSEs; (A) e-spinning technique to prepare HS-NFs, (B) SEM images of as e-spun TiO_2/polymer composite NFs, (C) the compression and thermal annealing step of the composite fibers to produce HS-NFs, (D) SEM images of the HS-NFs after calcination, (E) photo and chemical structures of the PC electrolyte, P14II-SN. (F) PC electrolyte injection step, the compression step was performed at 120 °C with pressure of 12.8 MPa. The thermal annealing was proceeded stepwise fashion at 150, 320, and 450 °C.

Scheme 1. Schematic Illustration of Formation of the HS-NFs (Nanorods-in-Nanofiber Morphology) during Thermal Annealing Process

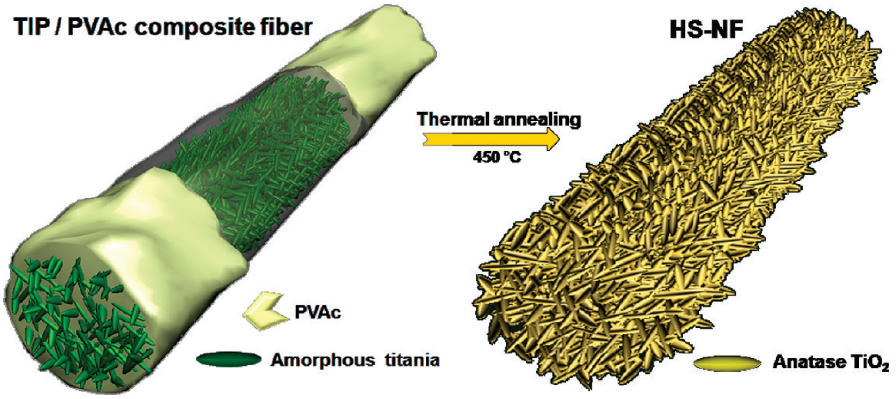

between the sample and a 450W Xe lamp. The intensity of the simulated light was calibrated by a Si reference solar cell equipped with a BK7 filter for approximating AM 1.5 global radiation. The photovoltaic characteristics of DSC were obtained by applying an external potential bias to the cells and measuring the generated photocurrent with a Keithley model 2400 source meter. The photovoltaic performance was measured by using black tapes with an aperture area of 0.164 cm^2. IPCE was measured as a function of wavelength from 350 nm to 800 nm using a specially designed IPCE system for dye-sensitized solar cell (PV measurement, Inc.). A 75 W xenon lamp was used as the light source for generating a monochromatic beam. Calibration was performed using a NIST-calibrated silicon photodiode as a standard. IPCE values were collected at a low chopping speed of 5 Hz. he electrical impedance spectra were measured using an impedance analyzer (Solatron 1260) at an open-circuit potential under AM 1.5 full sun illumination (100mW/cm^2), with a frequency range of 0.1−10^5 Hz. The magnitude of the alternative signal was 10 mV. Impedance parameters were determined by fitting of the impedance spectra using Z-plot software. The electron transport time and electron recombination lifetimes were measured by intensity-modulated photocurrent spectroscopy (IMPS) and intensity-modulated photovoltage spectroscopy (IMVS). A diode laser with variable power and modulation control (Coherent CUBE Diode-laser, 40mW, 445 nm) was used as the light source for these studies. Illumination was always incident on the working electrode side of the solar cells. The intensity was measured using a calibrated Si-photodiode. IMVS was performed under open-circuit conditions. The output of the solar cell was connected directly to a lock-in amplifier (Frequency Response Analyzers, Solatron 1260 Impedance/Gain - phase Analyzer). IMPS was performed by connecting the solar

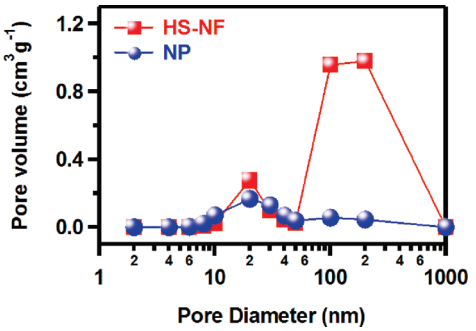

Figure 2. Pore volume distribution of HS-NF and TiO_2—NP as a function of pore diameter. The specific surface area was estimated using the BET analysis and the pore diameters were determined by the BJH analysis using the N_2 adsorption—desorption branches of the isotherms measured at −196 °C.

cell via a current amplifier (EG&G PAR 273) to the lock-in amplifier. During the IMVS and IMPS measurements, the cell was illuminated with sinusoidally modulated light having a small ac component (10% or less of the dc component).

RESULTS AND DISCUSSION

The HS-NF photoelectrodes were prepared by e-spinning a titanium(IV) propoxide (TIP)/poly(vinyl acetate) (PVAc) solution in dimethyl formamide (DMF) on to a fluorine-doped tin oxide (FTO) coated glass plate followed by thermal annealing at 450 °C in an air atmosphere. Figure 1A schematically depicts the e-spinning method utilized for the HS-NFs preparation. The in situ e-spun TIP/PVAc composite fibers (refer the SEM images in Figure 1B) were compressed under pressure of 12.8 MPa at 120 °C before thermal annealing (Figure 1C). This lamination step is essential to enhance the connectivity among the NFs and also the adhesion onto the FTO/glass substrate, controlling the pore volume of the final TiO_2 electrodes which will influence both the electron pathways and electrolyte infiltration. The selection of the titania precursors and matrix polymers, the ratio between the two components, and other processing conditions such as lamination and calcination can influence the morphology of the TiO_2—NFs.[33] Scheme 1 illustrates the possible formation mechanism for our TiO_2 HS-NFs from the TIP/PVAc composite fibers by thermal annealing. In the as-spun composite fibers, the amorphous titania were embedded in the matrix polymer. Upon subsequent thermal treatment at 450 °C in air, the amorphous titania were crystallized to anatase TiO_2 nanorods simultaneously removing the matrix polymer. As a result, the nanorod-in-nanofiber morphology was obtained. The SEM images of the HS-NFs photoelectrodes shown in Figure 1D are correspondent to the hierarchical morphology displayed in scheme 1. In these HS-NFs, low aspect ratio (<6) TiO_2 nanorods (~15 nm in diameter) are dendrited on the submicrometer scale (~500 nm) core TiO_2—NFs (enlarged SEM images in Figure 1D). The average length of the NFs containing a high density of nanorods ranges between 150—200 μm, thus retaining their connectivity. The morphology of HS-NFs was further investigated using Brunauer—Emmett—Teller (BET) analysis. Figure 2 shows the bimodal distribution of pores in the HS-NF electrodes. The macropores are generated by the interfiber space among the submicrometer scale core fibers and the mesopores are constructed by the inter-rod spaces among the nanorod dendrites (see the enlarged SEM images in Figure1D). The pore volume per gram of the HS-NFs was extraordinary high (2.41 cm^3 g^{-1}) compared to the conventional NPs (0.61 cm^3 g^{-1}). This much increased pore volume should allow improved electrolyte penetration. This high pore volume of HS-NFs is mainly contributed by macropores that could be manipulated by adjusting the compression force during the lamination step. The surface area per gram of the HS-NFs determined by BET was ~50% higher (112 m^{2}g^{-1}) than conventional NP based photoelectrodes (75.0 m^2 g^{-1}) affording enhanced dye loading.[25] The morphology analysis results of HS-NFs and conventional NPs determined by BET and the Barrett—Joyner—Halenda (BJH) methods are summarized in Table 1. It should be noted that the high pore volume of the HS-NFs was strategically determined for our PC-SSEs used in this study because the PC-SSEs exhibit higher viscosity than conventional liquid electrolytes and undesired solidification can often occur because of a change in temperature during the electrolyte filling.

Table 1. Physical Properties of the Photoelectrodes (TiO_2—NP and HS-NF) Obtained Using BET and BJH Methods

sample	surface area S (m^2 g^{-1})	cumulated pore volume V_p (cm^3 g^{-1})	porosity P (%)[a]	roughness factor R[b]
NP	75	0.61	70.3	83.3
HS-NF	112	2.41	90.4	43.7

[a] Porosity (P) is calculated by the formula; $P = V_p/(\rho^{-1} + V_p)$, where V_p is the specific pore volume and ρ is the density of the TiO_2. [b] Roughness factor (R) is calculated by the formula $R = \rho(1 - P)S$, where S is the specific surface area.

RT solid-state DSSCs were fabricated using a PC electrolyte. The PC-SSE was prepared by formulating a molecular PC, succinonitrile (SN), with N-methyl-N-butylpyrrolidinium iodide ($P_{14}I$) and I_2 as dopants to deliver enough ionic conductivity and sufficient kinetics for the dye reduction.[30] The three components were mixed at high temperature (~ 70 °C) followed by cooling to RT, and the molar ratio between SN/P_{14}I/I_2/ was 100/5/1. This PC electrolyte, which will be denoted as P14II-SN, preserved a PC phase between −40 and ~60 °C.[30,31] For DSSC assembly, the P14II-SN was liquefied by heating above 70 °C, and then injecting into the preassembled N719 dye-loaded cells. The rapid infiltration was crucial for successful cell fabrication because the P14II-SN rapidly solidifies on a small excursion to lower temperatures. Cooling to RT yielded the PC based solid-state DSSCs. In previous reports, P14II-SN exhibited high ionic conductivity (3.3 mScm^{-1}) and ion diffusion coefficients (3.7×10^{-6} cm^{2}s^{-1} for I^- and 2.2×10^{-6} cm^{2}s^{-1} for I_3^-) which are comparable to the high performance RT-IL based electrolytes.[30] These excellent properties for a solid state electrolyte are attributed to the efficient GEM, and this hopping based mechanism demands high concentration of ions (I^- and I_3^-) for effective charge transport. In our P14II-SN, 0.12 M of iodine, which is 5—10 times higher amount than the conventional organic liquid electrolytes was used.[1,34] Notably, this increased I_2 concentration generates a larger concentration of I_3^- ions which could potentially increase the charge recombination rate with the injected electrons in the TiO_2, resulting in reduced short circuit current (J_{SC}) and V_{OC}. Therefore, retarding the charge recombination rate is crucial to improving the performance of the solid-state

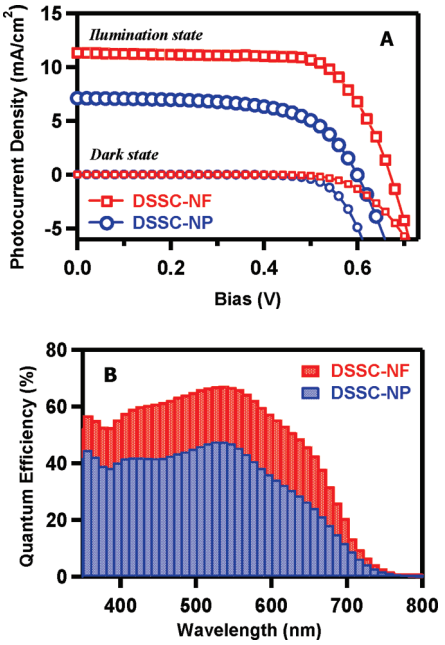

Figure 3. Photovoltaic properties of the solid-state DSSCs. (A) $J-V$ curves measured under simulated AM 1.5G light one sun condition, (B) incident photon to current conversion efficiency (IPCE) results.

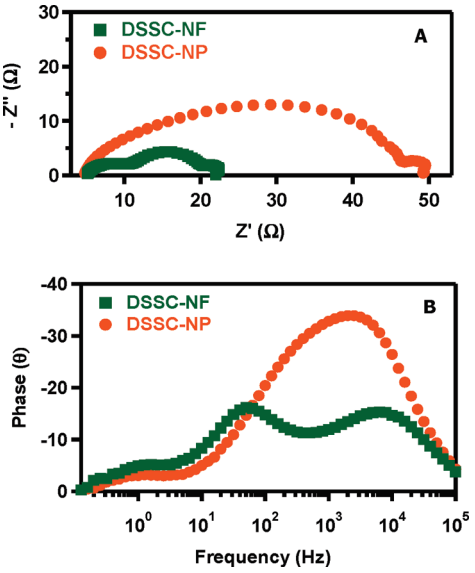

Figure 4. Electrochemical impedance spectroscopy (EIS) results of the DSSCs at open-circuit condition under simulated AM1.5G illumination; (A) Nyquist plots at a frequency range of 1×10^{-1} to approximately 1×10^{5} Hz, and (B) Bode phase plots.

Table 2. Summary of the Photovoltaic Properties of the Solid-State DSSCs Using TiO_2—NP and HS-NF-Based Photoelectrodes[a]

DSSCs	V_{OC} (mV)	J_{SC} (mA/cm^2)	FF (%)	PCE (%)
DSSC-NP (9 μm, 100 mW cm^{-2})	599	7.1	62.1	2.65%
DSSC-NF (9 μm, 100 mW cm^{-2})	670	11.3	71.2	5.41%
DSSC-NF (14 μm, 100 mW cm^{-2})[b]	668	14.1	69.3	6.54%
DSSC-NF (14 μm, 50 mW cm^{-2})[b]	651	8.7	67.8	7.69%
DSSC-NF (14 μm, 30 mW cm^{-2})[b]	630	5.6	67.5	7.93%

[a] The numbers in the brackets indicate the thickness of the photoelectrode layers and the AM 1.5G light intensity during the $J-V$ measurements. [b] Post treatment was performed by submerging the photoelectrodes in 0.02 M aqueous $TiCl_4$ for 20 min at 80 °C.

DSSCs, and creating a TiO_2 morphology that suppresses recombination is envisaged as an effective strategy.

Figure 3A shows the $J-V$ characteristics of the P14II-SN based solid-state DSSCs. The PCE of DSSC-NF (5.41%) was >2-fold higher than that of DSSC-NP (2.65%) with improved V_{OC}, J_{SC}, and fill factor (Table 2). Generally, the FF of the DSSCs is related to the magnitude of the series resistance element, R_s, which is composed of various components.[21] The R_s of the DSSCs was analyzed using electrochemical impendence spectroscopy (EIS) in order to understand the origin of the improved FF. Figure 4A shows the Nyquist plot of the DSSC-NF and DSSC-NP at open circuit under one sun illumination. The R_s values, determined from the real component (Z') of the DSSC-NF (23 Ω cm^2) was less than 1/2 of that of the DSSC-NP (49 Ωcm^2) as indicated in Figure 4A. This is attributed that the enhanced infiltration of P14II-SN into HS-NF containing a significant portion of macropores facilitates efficient hole transport and dye regeneration. As shown in the Bode plot (Figure 4B), the maximum of the middle frequency range, was much lower in DSSC-NFs (~50 Hz) than that of DSSC-NPs (~800 Hz) indicating the reduced charge recombination rate. The effect of the improved charge recombination lifetime in DSSC-NFs will be further discussed in the following section.

The enhanced J_{SC} and incident photon to current efficiency (IPCE) of DSSC-NFs is indicated in Figure 3A and 3B. The photocurrent density of DSSCs is determined by the efficiencies of (i) light harvesting, (ii) charge injection, and (iii) charge collection.[35−37] The light harvesting efficiency is a strong function of the dye loading, which in turn is correlated to the roughness factor (R) of the photoelectrodes. R is determined by the relation $R = \rho(1 - P)S$, where ρ is density of TiO_2, P is porosity, and S is the surface area per gram. The HS-NFs exhibits much lower R than NPs as shown in Table 1.[38,39] The much higher porosity of HS-NFs is responsible for the lower R value in spite of the higher surface area per gram. This was a surprising result that the J_{sc} of DSSC-NFs was higher although the HS-NFs can harvest less light than NPs. Therefore, the elevated photocurrent density of the DSSC-NFs is possibly dependent on the charge collection efficiency (η_{cc}) because the charge injection efficiency from N719 dye to the TiO_2 is near unity.[22,40]

The η_{cc} of DSSCs is determined by the relation; $\eta_{cc} = 1 - (\tau_{ct}/\tau_r)$ where τ_{ct} is a charge transport time and τ_r is a charge recombination lifetime.[36−42] The τ_{ct} was obtained using intensity modulation photocurrent spectroscopy (IMPS). The frequency of incident light modulation was ranged from 100 to 0.1 Hz in our experiments. The τ_{ct} as a function of the incident light intensity is plotted in Figure 5A. The τ_{ct} of the DSSC-NFs was slightly shorter than that of the DSSC-NPs. This is attributed to the lower junction density of the 1D nanostructured HS-NFs, although the much higher pore volume also offers an additionally tortuous route for the charge transport.[25,38] The intrinsically superior charge transport properties of the NFs could compensate for the longer transport path of the highly porous TiO_2 layers that is beneficial for electrolyte infiltration displaying the shorter

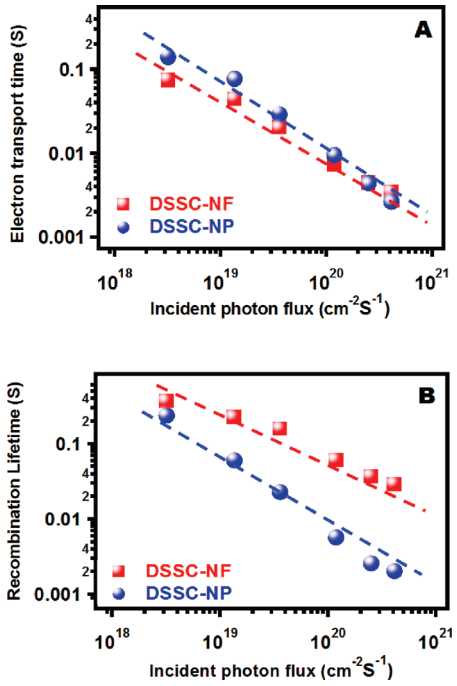

Figure 5. Evolution of electron transport time and recombination lifetime of DSSC-NFs and DSSC-NPs as a function of incident photon flux by frequency resolved techniques; (A) IMPS and (B) IMVS results. The thickness of the TiO_2 photoelectrodes for both types of DSSCs was ~9 μm.

net charge transporting time. The τ_r was obtained using intensity modulated photovoltage spectroscopy (IMVS). The τ_r values can be calculated from the relation: $\eta_{cc} = 1/2\pi f_{min(IMVS)}$, where f_{min} is the minimum voltage of the imaginary part of the low-frequency range in IMVS. On the basis of the IMVS results shown in Figure 5B, the τ_r of DSSC-NF was ~14 times longer than that of the DSSC-NP at incident photon flux = 4.10×10^{20} cm^{-2} s^{-1}. The η_{cc} of DSSC-NFs determined by the frequency-resolved techniques were >40% greater than that of DSSC-NPs. This enhanced η_{cc} in DSSC-NFs was mainly attributed to the superior charge recombination lifetime. This is due to the fact that our 1D HS-NFs retain a reduced junction density where charge trapping events typically occur. The enhanced charge collection efficiency that results from the longer recombination lifetime is therefore the major cause of the enhanced J_{sc} of the DSSC-NFs.

It is noteworthy that the τ_r difference in DSSC-NF and DSSC-NP using P14II-SN SSEs was extraordinary although the improved τ_r at 1D structured TiO_2 based DSSCs using conventional organic liquid electrolytes has been reported by several groups including our group.[22,24,28] In our earlier work, approximately eight times longer τ_r was demonstrated in DSSCs using a similar TiO_2—NFs and an organic liquid electrolyte,[25] which was concordant with other reported results.[26−29] We attribute the striking elevation of the τ_r in the DSSC-NFs to the nature of our PC based SSEs. The P14II-SN contains >5 times higher I_2 concentration than conventional organic liquid electrolytes, because the high I_3^- concentration is necessary for efficient ion transport through the GEM. As a result however, the unwanted charge recombination between the electrons on the TiO_2 and I_3^- may be enhanced in addition to greater visible light absorption in the electrolyte.[43] The effect of retarding charge recombination rate by our HS-NFs is thus much more significant in the PC-SSEs than in conventional organic liquid electrolytes.

The extraordinarily long τ_r of HS-NFs was reflected in the V_{OC} of the DSSC-NFs (Figure 5B and Table 2). Since the value of V_{OC} is determined by the energy level difference between the reduction potential of the electrolyte and the quasi Fermi level of the TiO_2, an increment of the electron density in the TiO_2 conduction band can shift the location of the TiO_2 quasi Fermi level to more negative potentials, elevating the V_{OC} value. The photoelectron density (PED) of the TiO_2 conduction band is proportional to the J_{SC} and τ_r.[44] On the basis of this relationship, the PED of DSSC-NFs was estimated to be >20 times higher than that of DSSC-NPs. This enhanced PED of DSSC-NFs raises the V_{OC} value by >70 mV compared to DSSC-NP. The higher V_{OC} in DSSC-NFs can also be confirmed in the EIS results. The maximum frequency (ω_{max}) at the middle range of bode phase plots (Figure 4B) for DSSC-NFs was much lower than those for DSSC-NPs, which is reliable with the tendency of the inverse V_{OC}. Under the illumination state, the V_{OC} related to the recombination lifetime can be described in eq 1

$$V_{OC} = \frac{RT}{\beta F}\ln\left(\frac{AI}{n_o k_1 [I_3^-] + n_o k_2 [D^+]}\right) \quad (1)$$

where R is the molar gas constant, T is the temperature, F is the Faraday constant, β is the reaction order for I_3^- and electrons, A is the electrode area, I is the incident photon flux, n_o is the concentration of accessible electronic states in the conduction band and k_1 and k_2 are the kinetic constant of the back reaction of the injected electrons with I_3^- and the recombination of these electrons with oxidized dyes (D^+), respectively. Assuming that the recombination with the oxidized dye molecules can be neglected, the V_{OC} will depend logarithmically on the kinetic constant of the back reaction of the injected electrons with I_3^- (k_1). Because the concentration of I_3^- in electrolyte and incident photon flux were constant under our experimental conditions, the V_{OC} is proportional to $\ln(1/\omega_{max})$, which demonstrates that the charge recombination rate influence the V_{OC} of DSSCs significantly. This EIS results are in accordance with the IMVS results.

Finally, the performance of the solid-state DSSC-NF was improved by optimizing the thickness of the HS-NF photoelectrodes. The PCE was improved to 6.54% with V_{OC} of 668 mV, J_{sc} of 14.1 mA cm^{-2}, and FF of 69.3% at AM 1.5G (100 mW cm^{-2}). At lower light intensity, the PCE was increased to 7.93% (30 mW cm^{-2}) (Table 2 and Figure S1 in the Supporting Information). This is a significant improvement from the previously reported values (~5% at 100 mW cm^{-2}), and by far, to the best of our knowledge, the highest values of the DSSCs using PC based SSEs. Further optimization of the cell performance can also be envisioned using additives and/or other post treatments.

CONCLUSIONS

In summary, high-performance RT solid-state DSSCs were demonstrated using 1D hierarchically structured TiO_2 and PC-SSEs. The strategic manipulation of the morphology of the TiO_2 photoelectrode layers improved the PCE of the DSSCs remarkably. The well-interconnected nanorod-in-nanofiber morphology of HS-NFs was beneficial for the infiltration of the PC-SSEs and efficient charge collection. The interfiber space offered a controlled degree of macroporosity and the continuity of the interconnected 1D HS-NFs provide good charge transport characteristics with extraordinarily long charge recombination lifetime. Notably, this morphology was particularly effective for

the PC-SSEs because the intrinsically high charge recombination probability (due to the high concentration of iodine present) was significantly retarded. This reduced charge recombination rate resulted in *a* >2-fold enhancement in the PCE in DSSC-NFs compared to the conventional DSSC-NPs. The optimized PCE of DSSC-NF was 7.93%. This is, by far the best performance among RT solid-state DSSCs using PC electrolytes, indicating that our HS-NFs are a promising morphology for SSEs generally. This morphological effect can be envisioned for the other electrolyte systems such as RT-IL based electrolytes which use high concentrations of iodine because the GEM is the major ion transporting protocol. The HS-NF based DSSCs using nonvolatile RT-IL-based electrolytes and other SSEs is currently under development in our group.

■ ASSOCIATED CONTENT

Supporting Information. SEM image of HS-NFs after dye loading, $J-V$ characterization results of DSSC-NFs, and photovoltaic properties of DSSC-NFs with respect to light intensities. This material is available free of charge via the Internet at http://pubs.acs.org.

■ AUTHOR INFORMATION

Corresponding Author

*E-mail: syjang@kookmin.ac.kr. Tel: +82- 2- 910- 5768. Fax: +82- 2- 910- 4415.

Present Addresses

[§]Department of Chemistry, Kookmin University, Seoul, Korea.

■ ACKNOWLEDGMENT

The authors gratefully acknowledge the support from the KIST Program, the Korea Research Council of Fundamental Science & Technology (KRCF) and KIST for 'National Agenda Project (NAP)' program.

■ REFERENCES

(1) Gao, F.; Wang, Y.; Shi, D.; Zhang, J.; Wang, M.; Jing, X.; Humphry-Baker, R.; Wang, P.; Zakeeruddin, S. M.; Grätzel, M. *J. Am. Chem. Soc.* **2008**, *130*, 10720–10728.

(2) Wang, P.; Zakeeruddin, S. M.; Moser, J. E.; Nazeeruddin, M. K.; Sekiguchi, T.; Grätzel, M. *Nat. Mater.* **2003**, *2*, 402–407.

(3) Wang, P.; Zakeeruddin, S. M.; Comte, P.; Exnar, I.; Grätzel, M. *J. Am. Chem. Soc.* **2003**, *125*, 1166–1167.

(4) Stergiopoulos, T.; Arabatzis, I. M.; Katsaros, G.; Falaras, P. *Nano Lett.* **2002**, *2*, 1259–1261.

(5) Snaith, H. J.; Moule, A. J.; Klein, C.; Meerholz, K.; Friend, R. H.; Grätzel, M. *Nano Lett.* **2007**, *7*, 3372–3376.

(6) Wu, J.; Hao, S.; Lan, Z.; Lin, J.; Huang, M.; Huang, Y.; Li, P.; Yin, S.; Sato, T. *J. Am. Chem. Soc.* **2008**, *130*, 11568–11569.

(7) Fabregat-Santiago, F.; Bisquert, J.; Cevey, L.; Chen, P.; Wang, M.; Zakeeruddin, S. M.; Grätzel, M. *J. Am. Chem. Soc.* **2008**, *131*, 558–562.

(8) Bach, U.; Lupo, D.; Comte, P.; Moser, J. E.; Weissortel, F.; Salbeck, J.; Spreitzer, H.; Grätzel, M. *Nature* **1998**, *395*, 583–585.

(9) Snaith, H.; Grätzel, M. *Adv. Mater.* **2007**, *19*, 3643–3647.

(10) Liu, X.; Zhang, W.; Uchida, S.; Cai, L.; Liu, B.; Ramakrishna, S. *Adv. Mater.* **2010**, *22*, E150–E155.

(11) Wang, M.; Yin, X.; Xiao, X. R.; Zhou, X.; Yang, Z. Z.; Li, X. P.; Lin, Y. *J. Photochem. Photobiol., A* **2008**, *194*, 20–26.

(12) Huo, Z.; Dai, S.; Zhang, C.; Kong, F.; Fang, X.; Guo, L.; Liu, W.; Hu, L.; Pan, X.; Wang, K. *J. Phys. Chem. B* **2008**, *112*, 12927–12933.

(13) Freitas, F. S.; Freitas, J. N. d.; Ito, B. I.; Paoli, M.-A. D.; Nogueira, A. F. *ACS Appl. Mater. Interfaces* **2009**, *1*, 2870–2877.

(14) Winther-Jensen, O.; Armel, V.; Forsyth, M.; MacFarlane, D. R. *Macromol. Rapid Commun.* **2010**, *31*, 479–483.

(15) Kim, J. H.; Kang, M.-S.; Kim, Y. J.; Won, J.; Park, N.-G.; Kang, Y. S. *Chem. Commun.* **2004**, *14*, 1662–1663.

(16) Han, H.; Liu, W.; Zhang, J.; Zhao, X. Z. *Adv. Funct. Mater.* **2005**, *15*, 1940–1944.

(17) Bai, Y.; Cao, Y.; Zhang, J.; Wang, M.; Li, R.; Wang, P.; Zakeeruddin, S. M.; Grätzel, M. *Nat. Mater.* **2008**, *7*, 626–630.

(18) Kroeze, J. E.; Hirata, N.; Koops, S.; Nazeeruddin, M. K.; Schmidt-Mende, L.; Grätzel, M.; Durrant, J. R. *J. Am. Chem. Soc.* **2006**, *128*, 16376–16383.

(19) Kubo, W.; Kambe, S.; Nakade, S.; Kitamura, T.; Hanabusa, K.; Wada, Y.; Yanagida, S. *J. Phys. Chem. B* **2003**, *107*, 4374–4381.

(20) Cao, Y.; Zhang, J.; Bai, Y.; Li, R.; Zakeeruddin, S. M.; Grätzel, M.; Wang, P. *J. Phys. Chem. C* **2008**, *112*, 13775–13781.

(21) Jiu, J.; Isoda, S.; Wang, F.; Adachi, M. *J. Phys. Chem. B* **2006**, *110*, 2087–2092.

(22) Zhu, K.; Neale, N. R.; Miedaner, A.; Frank, A. J. *Nano Lett.* **2006**, *7*, 69–74.

(23) Adachi, M.; Murata, Y.; Takao, J.; Jiu, J.; Sakamoto, M.; Wang, F. *J. Am. Chem. Soc.* **2004**, *126*, 14943–14949.

(24) Kang, S. H.; Choi, S.-H.; Kang, M.-S.; Kim, J.-Y.; Kim, H.-S.; Hyeon, T.; Sung, Y.-E. *Adv. Mater.* **2008**, *20*, 54–58.

(25) Lee, B. H.; Song, M. Y.; Jang, S.-Y.; Jo, S. M.; Kwak, S.-Y.; Kim, D. Y. *J. Phys. Chem. C* **2009**, *113*, 21453–21457.

(26) Law, M.; Greene, L. E.; Johnson, J. C.; Saykally, R.; Yang, P. *Nat. Mater.* **2005**, *4*, 455–459.

(27) Kongkanand, A.; Martínez Domínguez, R.; Kamat, P. V. *Nano Lett.* **2007**, *7*, 676–680.

(28) Mor, G. K.; Shankar, K.; Paulose, M.; Varghese, O. K.; Grimes, C. A. *Nano Lett.* **2005**, *6*, 215–218.

(29) Archana, P. S.; Jose, R.; Vijila, C.; Ramakrishna, S. *J. Phys. Chem. C* **2009**, *113*, 21538–21542.

(30) Wang, P.; Dai, Q.; Zakeeruddin, S. M.; Forsyth, M.; MacFarlane, D. R.; Grätzel, M. *J. Am. Chem. Soc.* **2004**, *126*, 13590–13591.

(31) Dai, Q.; MacFarlane, D. R.; Howlett, P. C.; Forsyth, M. *Angew. Chem.* **2005**, *44*, 313–316.

(32) Chen, Z.; Yang, H.; Li, X.; Li, F.; Yi, T.; Huang, C. *J. Mater Chem.* **2007**, *17*, 1602–1607.

(33) Ahn, Y. R.; Song, M. Y.; Jo, S. M.; Park, C. R.; Kim, D. Y. *Nanotechnology* **2006**, *17*, 2865–2869.

(34) Li, R.; Liu, J.; Cai, N.; Zhang, M.; Wang, P. *J. Phys. Chem. B* **2010**, *114*, 4461–4464.

(35) Ghadiri, E.; Taghavinia, N.; Zakeeruddin, S. M.; Grätzel, M.; Moser, J.-E. *Nano Lett.* **2010**, *10*, 1632–1638.

(36) Schlichthorl, G.; Park, N. G.; Frank, A. J. *J. Phys. Chem. B* **1999**, *103*, 782–791.

(37) Jennings, J. R.; Ghicov, A.; Peter, L. M.; Schmuki, P.; Walker, A. B. *J. Am. Chem. Soc.* **2008**, *130*, 13364–13372.

(38) Benkstein, K. D.; Kopidakis, N.; van de Lagemaat, J.; Frank, A. J. *J. Phys. Chem. B* **2003**, *107*, 7759–7767.

(39) van de Lagemaat, J.; Benkstein, K. D.; Frank, A. J. *J. Phys. Chem. B* **2001**, *105*, 12433–12436.

(40) Katoh, R.; Furube, A.; Hara, K.; Murata, S.; Sugihara, H.; Arakawa, H.; Tachiya, M. *J. Phys. Chem. B* **2002**, *106*, 12957–12964.

(41) Haque, S. A.; Palomares, E.; Cho, B. M.; Green, A. N. M.; Hirata, N.; Klug, D. R.; Durrant, J. R. *J. Am. Chem. Soc.* **2005**, *127*, 3456–3462.

(42) Bisquert, J. *J. Phys. Chem. B* **2001**, *106*, 325–333.

(43) Yu, Z.; Gorlov, M.; Nissfolk, J.; Boschloo, G.; Kloo, L. *J. Phys. Chem. C* **2010**, *114*, 10612–10620.

(44) Schlichthorl, G.; Huang, S. Y.; Sprague, J.; Frank, A. J. *J. Phys. Chem. B* **1997**, *101*, 8141–8155.